nature physics

LETTERS

https://doi.org/10.1038/s41567-021-01476-w

Check for updates

# Realizing discontinuous quantum phase transitions in a strongly correlated driven optical lattice

Bo Song[1], Shovan Dutta[1], Shaurya Bhave[1], Jr-Chiun Yu[1], Edward Carter[1], Nigel Cooper[1,2] and Ulrich Schneider[1]✉

**Discontinuous (first-order) quantum phase transitions and the associated metastability play central roles in diverse areas of physics, ranging from ferromagnetism to the false-vacuum decay in the early Universe[1,2]; yet, their dynamics are not well understood. Ultracold atoms provide an ideal platform for experimental simulations of quantum phase transitions[3,4]; so far, however, studies of first-order phase transitions have been limited to systems with weak interactions[5–8], where quantum effects are exponentially suppressed. Here we realize a strongly correlated driven many-body system whose transition can be tuned from continuous to discontinuous. Resonant shaking of a one-dimensional optical lattice hybridizes the two lowest Bloch bands[9,10], driving a novel transition from a Mott insulator to a superfluid with a staggered phase order. For weak shaking amplitudes, this transition is discontinuous and the system can remain frozen in a metastable state, whereas for strong shaking, it undergoes a continuous transition towards a superfluid. Our observations of this metastability and hysteresis agree with numerical simulations and pave the way for exploring the crucial role of quantum fluctuations in discontinuous transitions.**

Phase transitions are ubiquitous in physics, ranging from thermal phenomena such as the boiling of water to magnetic transitions in solids and from cosmological phase transitions in the early Universe[11] to the transition into a quark–gluon plasma in high-energy collisions[12]. Particularly intriguing are quantum phase transitions that occur at temperatures close to absolute zero and are driven by quantum rather than thermal fluctuations[13]. So far, the focus has been on continuous quantum phase transitions (second order or higher), such as most magnetic or superfluid-to-Mott-insulator transitions. There is, however, a renewed interest in discontinuous (first-order) quantum phase transitions that are characterized by an inherent metastability where the system can remain in its initial phase after crossing the transition[14]. It is particularly interesting to understand the quantum decay of such a metastable state, termed false-vacuum decay, which is relevant in particle physics and cosmology as an analogue of the 'Big Bang' in inflationary universes[1,2,15–17].

Ultracold atoms in optical lattices provide a pristine and controllable platform to investigate quantum phases and phase transitions in isolated many-body systems. Although continuous phase transitions have been extensively studied in these systems[3,4], discontinuous transitions have so far been limited to weakly interacting condensates[5–8], for which the quantum decay of a metastable state is strongly suppressed: it requires the collective tunnelling of all the atoms within a healing length, leading to an exponential reduction, analogous to the suppression of tunnelling in large-spin systems[18]. Here, in contrast, we engineer a discontinuous quantum phase transition from a strongly interacting Mott insulator (MI) to a superfluid (SF) in a resonantly driven one-dimensional (1D) optical lattice[10]. Then, quantum fluctuations play an important role, analogous to their effects in small-spin systems such as in a spin-1/2 quantum XY model[19].

Our approach is based on periodically modulating or shaking the position of the lattice[10]. Off-resonant shaking is central for generating topological band structures[20] and can drive the conventional continuous Mott transitions by renormalizing tunnelling[10,21–23]. Resonant shaking, in contrast, coherently couples the two lowest Bloch bands and has been demonstrated in weakly interacting systems, where it results in spontaneous symmetry breaking[24] analogous to a ferromagnetic quantum phase transition[25].

In the present work, the parameters of the undriven lattice are chosen such that the many-body ground state in the lowest band is an MI, but the far stronger tunnelling in the first excited band alone would result in an SF state. We term this state as the π-SF state, as the negative sign of tunnelling implies that condensation occurs at the edge of the Brillouin zone, that is, with a staggered phase order. In the presence of a near-resonant drive, the corresponding dressed bands will cross, and we can drive the MI-to-π-SF transition by ramping the shaking frequency and therefore shifting the relative energies of the bands. Crucially, this transition is discontinuous at weak coupling strengths, because the non-staggered correlations in the MI are incompatible with the staggered order of the π-SF[9,26]. For stronger coupling strengths, on the other hand, the bands are strongly hybridized and the transition becomes continuous.

## Experimental setup

A Bose–Einstein condensate of around $10^5$ rubidium ($^{87}$Rb) atoms is adiabatically loaded into a three-dimensional simple-cubic lattice with lattice depths of $(V_x, V_y, V_z) = (33, 8.4, 49)E_r$, where $E_r = \frac{\hbar^2 k_0^2}{2m}$ denotes the recoil energy, $m$ is the mass of $^{87}$Rb, $\hbar$ is the reduced Planck constant, $k_0 = \frac{2\pi}{\lambda}$ and $\lambda = 726\,\mathrm{nm}$ is the wavelength of the lattice light. The lattices along $x$ and $z$ are sufficiently deep such that tunnelling along those directions is negligible and the cloud becomes partitioned into independent tubes along the $y$ direction, forming independent 1D MIs. The atoms are held in this static lattice for 10–15 ms before we start modulating (shaking) the position of the $y$ lattice by sinusoidally changing the corresponding laser frequency with modulation frequency $f$ using an acousto-optical modulator in

[1]Cavendish Laboratory, University of Cambridge, Cambridge, UK. [2]Department of Physics and Astronomy, University of Florence, Sesto Fiorentino, Italy. ✉e-mail: uws20@cam.ac.uk

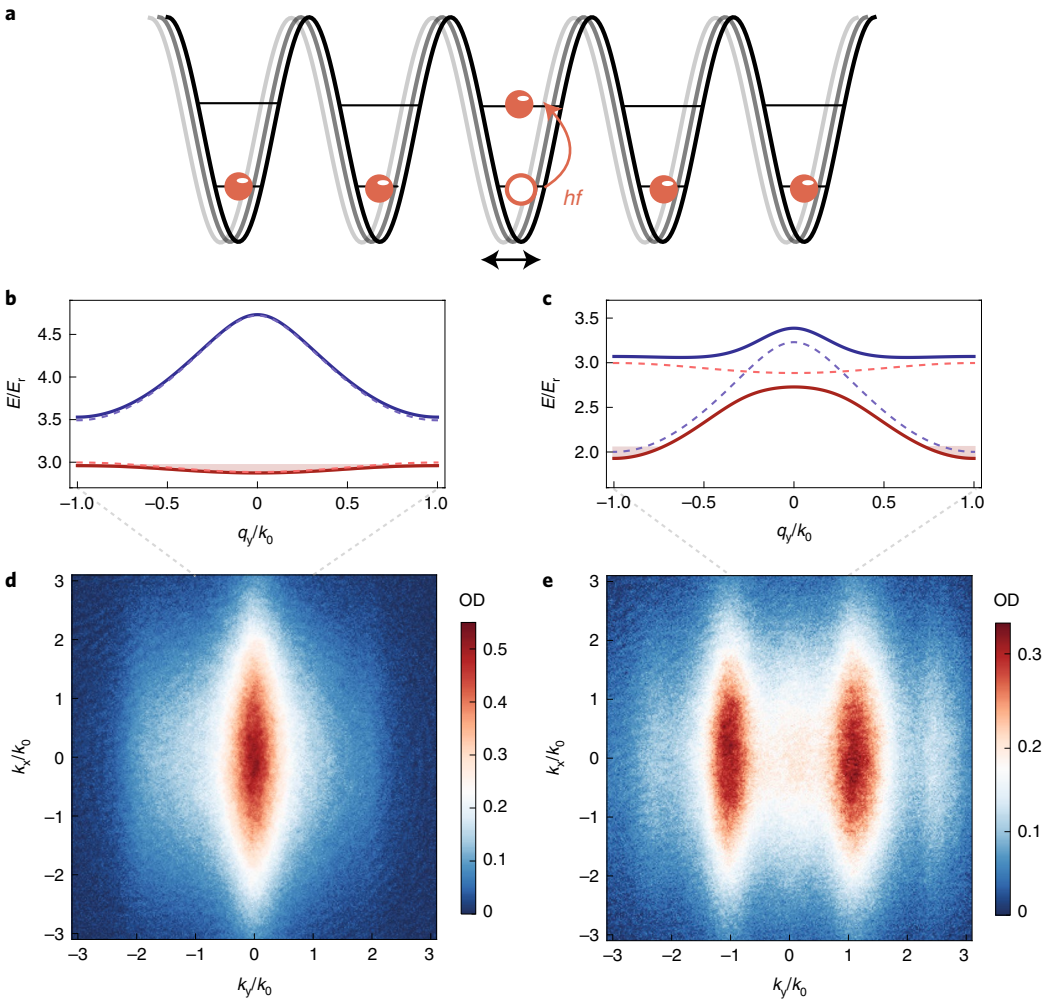


**Fig. 1 | Schematic of the shaken lattice. a**, Resonant modulation (shaking) of the lattice position hybridizes the two lowest single-particle Bloch bands. **b**,**c**, The two lowest dressed bands in the MI (off-resonant) and π-SF (resonant) regimes with shaking parameters $f$ and $\mathcal{A}$ of 15.0 kHz and 11.5 nm (**b**) and 21.5 kHz and 11.5 nm (**c**). The dashed lines indicate the bare (uncoupled) bands. While the momentum distribution of the MI in the lowest band is centred at around zero, the π-SF is quasi-condensed at the boundary of the Brillouin zone. **d**,**e**, Average time-of-flight images ($t_{tof}$ = 16 ms, OD: optical density) of the atoms released from the shaken lattice corresponding to **b** (**d**) and **c** (**e**), following the direct-sweep protocol depicted in Fig. 2a.

the double-pass configuration. Due to the retro-reflected setup, this translates to a spatial shaking of the lattice at the atoms' position. The shaking amplitude $\mathcal{A}$ and resulting coupling strength $\Omega \propto f^2\mathcal{A}$ between the two lowest bands are determined by the frequency modulation depth and distance ($l_0 \approx 45$ cm) between the atoms and retro-reflector (Methods). As the size of the atomic cloud is negligible compared with $l_0$, the shaking amplitude remains constant across the cloud.

Compared with off-resonant shaking schemes[22,23,27], typical amplitudes in this resonant case are tiny, namely, less than 4% of the lattice constant $d = \lambda/2$, such that the dressed and bare bands (Fig. 1b, solid and dashed lines) essentially coincide away from resonance. For resonant drives, on the other hand, the two bands hybridize and therefore strongly increase the bandwidth of the relevant dressed band (Fig. 1c, red).

## Extended Bose–Hubbard model

In the lattice frame, the shaking gives rise to an oscillatory force in the $y$ direction[28]. Expanding the field operator in terms of Wannier functions in the two lowest bands and moving to the rotating frame, one finds an effective Hamiltonian for sufficiently deep lattices (Methods),

$$\hat{H} = \sum_{\langle i,j\rangle} J_b \hat{b}_i^\dagger \hat{b}_j - J_a \hat{a}_i^\dagger \hat{a}_j + \sum_j \Delta \hat{b}_j^\dagger \hat{b}_j + \frac{\Omega}{2}\left(\hat{a}_j^\dagger \hat{b}_j + \hat{b}_j^\dagger \hat{a}_j\right) + \sum_j \frac{U_a}{2}\hat{a}_j^\dagger \hat{a}_j^\dagger \hat{a}_j \hat{a}_j + \frac{U_b}{2}\hat{b}_j^\dagger \hat{b}_j^\dagger \hat{b}_j \hat{b}_j + V \hat{a}_j^\dagger \hat{b}_j^\dagger \hat{b}_j \hat{a}_j \,, \quad (1)$$

where $\hat{a}_j$ and $\hat{b}_j$ represent bosonic annihilation operators in the ground and first-excited uncoupled bands, respectively; $J_b \gg J_a$ are the nearest-neighbour tunnelling in the two bands; and $U_{a,b}$ and $V$ are the intraband and interband on-site interactions, respectively. Due to the tiny shaking amplitudes, these parameters remain virtually unchanged in the shaken system. The effective detuning $\Delta = \Delta_E - hf$ is measured with respect to the average gap $\Delta_E$ between the two lowest bands and $h$ is Planck's constant. In our numerical simulations based on the density matrix renormalization group (DMRG)[29], we also add next-nearest-neighbour tunnelling in the excited band (which is comparable to $J_a$) and corrections of the order $1/f$ from the Floquet theory[30] (Methods). These additional terms do not significantly affect the results. Additionally, we have performed three-band simulations showing that higher bands are off-resonant

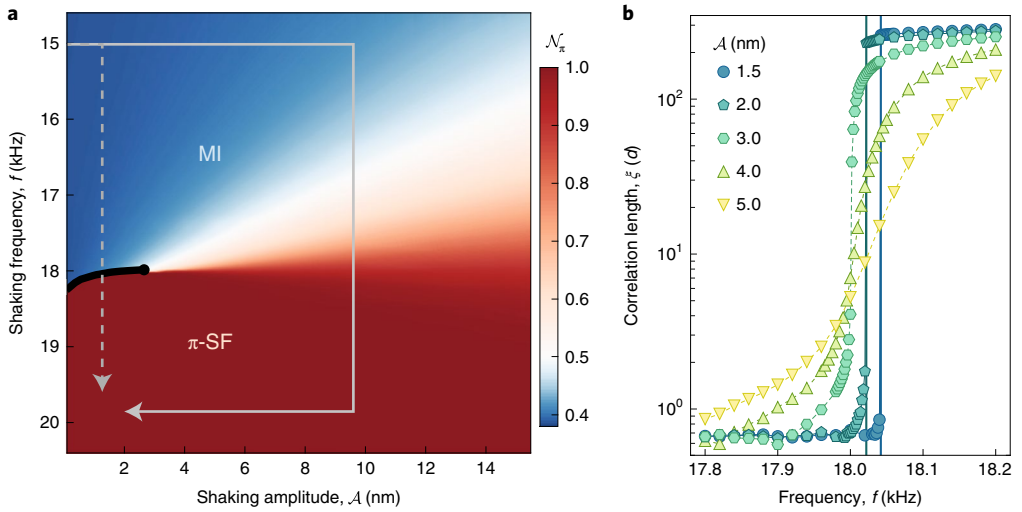


**Fig. 2 | Simulated phase diagram of the shaken lattice. a**, Normalized occupation $\mathcal{N}_\pi$ around momentum $\pm\hbar k_0$. For small shaking amplitudes $\mathcal{A}$, the MI (blue) and π-SF (red) phases are separated by an abrupt discontinuous transition (black solid line), which turns continuous for $\mathcal{A} \gtrsim 2.8$ nm. The grey arrows indicate the direct (dashed) and indirect (solid) sweeps used in Fig. 3. **b**, The distinction between the two types of phase transition is also reflected by the ground-state correlation length $\xi$. In contrast to weak amplitudes, where $\xi$ discontinuously jumps at the phase boundary, it smoothly varies for large $\mathcal{A}$. Here $\xi$ is calculated by averaging $\langle \hat{b}_i^\dagger \hat{b}_j \rangle$, obtained from a two-band DMRG with 64 sites and unity filling, over the bulk (Methods).

and unimportant for the used experimental sweeps (Supplementary Fig. S5). Although higher bands would become significant for much slower large-amplitude sweeps, they can be suppressed using superlattice techniques[9].

## Phases and their signatures

The scenario in equation (1) was first discussed in ref. [9] and can be interpreted as a frustrated ladder model, as the tunnelling elements in the two bands have opposite signs. Consequently, a many-body state can either satisfy the links in the ground band or the links in the excited band, but not both at the same time. This frustrated hopping is at the heart of the discontinuous phase transition. For weak coupling strengths in the discontinuous regime, either the ground or excited band is almost exclusively occupied depending on detuning $\Delta$. In the ground band, the interaction energy dominates over the kinetic energy and the system forms an MI with small and positive nearest-neighbour correlations $\langle \hat{a}_i^\dagger \hat{a}_{i+1} \rangle > 0$. In the excited band, in contrast, the larger bandwidth implies that kinetic energy dominates and the system is in a π-SF state, where the negative sign of hopping results in a staggered order with $\langle \hat{b}_i^\dagger \hat{b}_{i+1} \rangle < 0$. As there can be no continuous transition connecting these two incompatible orders, the system has to choose one of them, giving rise to a discontinuous transition. Conversely, strong coupling results in strongly hybridized bands, where the transition from positive to negative nearest-neighbour correlations (from non-staggered to staggered) already happens within the MI regime. The phase transition now smoothly connects a staggered MI to a staggered π-SF and is of the normal continuous Kosterlitz–Thouless (KT) type, see Methods and Extended Data Figs. 1 and 2 for details.

These phases exhibit distinct signatures in the momentum distribution measured by time-of-flight imaging, as shown in Fig. 1d,e. In the initially prepared (non-staggered) MI, the broad momentum distribution is centred at around $k=0$ (Fig. 1d) and the absence of satellite peaks demonstrates the absence of long-range coherence. Conversely, in the π-SF, the atoms are concentrated around $k=\pm k_0$ (Fig. 1e), and the relatively narrow satellite peaks at higher momenta signal the presence of at least short-range coherence. To distinguish between these phases, we extract the normalized population at the band edge, namely, $\mathcal{N}_\pi := n_\pi/(n_0 + n_\pi)$, by counting the number of atoms in fixed windows around $k=0$ (for $n_0$) and $k=\pm k_0$ (for $n_\pi$) (Methods).

Figure 2a shows the simulated phase diagram (for the effective Hamiltonian) at unity filling. For weak shaking amplitudes, $\mathcal{N}_\pi$ changes abruptly with shaking frequency $f$, indicating the discontinuous phase transition. Beyond a critical drive amplitude of $\mathcal{A}_c \simeq 2.8$ nm, the change in $\mathcal{N}_\pi$ becomes smooth as the phase transition turns continuous. This change from discontinuous to continuous is further corroborated by the vanishing of the jump in the simulated one-body correlation lengths (Fig. 2b) and the behaviour of the entanglement entropy presented in Methods. In a mean-field picture, in contrast, the transition remains discontinuous, highlighting the critical role of quantum fluctuations in reducing the barrier height between the MI and π-SF phases.

## Dynamics of phase transition and quantum metastability

The discontinuous nature and associated metastability are revealed by comparing two different frequency sweeps (termed direct and indirect sweeps) indicated by arrows in Fig. 2a. In the direct sweep, the shaking amplitude is linearly increased from 0 to the final amplitude in 125 μs at a fixed off-resonant frequency of 15 kHz before the shaking frequency is linearly increased to the final frequency in 600 μs. In the indirect sweep, first the shaking amplitude is linearly increased from 0 to a common large amplitude of $\mathcal{A}=9.6$ nm in 125 μs at 15 kHz. Then, the shaking frequency is linearly swept to the final frequency in 600 μs before the shaking amplitude is decreased to the final amplitude in 300 μs, see also Extended Data Fig. 3. The indirect-sweep protocol ensures that the system always undergoes a continuous phase transition, circumventing the discontinuous regime. For these indirect sweeps, the atoms largely remain in the original of the two dressed bands (Fig. 1b,c, red solid line) and, for sufficiently slow sweeps, stay close to the ground state[31].

Figure 3 shows the state at the end of the sweeps as a function of the final amplitude and frequency. Although the results for the indirect sweeps (Fig. 3c,d) agree well with the static phase diagram shown in Fig. 2a, the direct sweeps (Fig. 3a,b) clearly demonstrate the metastable nature of the discontinuous phase transition: in the discontinuous regime, the system remains in the initial MI state characterized by small $\mathcal{N}_\pi$, even though the ground state changes to the π-SF state.

Next, we further investigate the dynamics of phase transition by varying the duration of direct frequency sweeps. Figure 4a shows

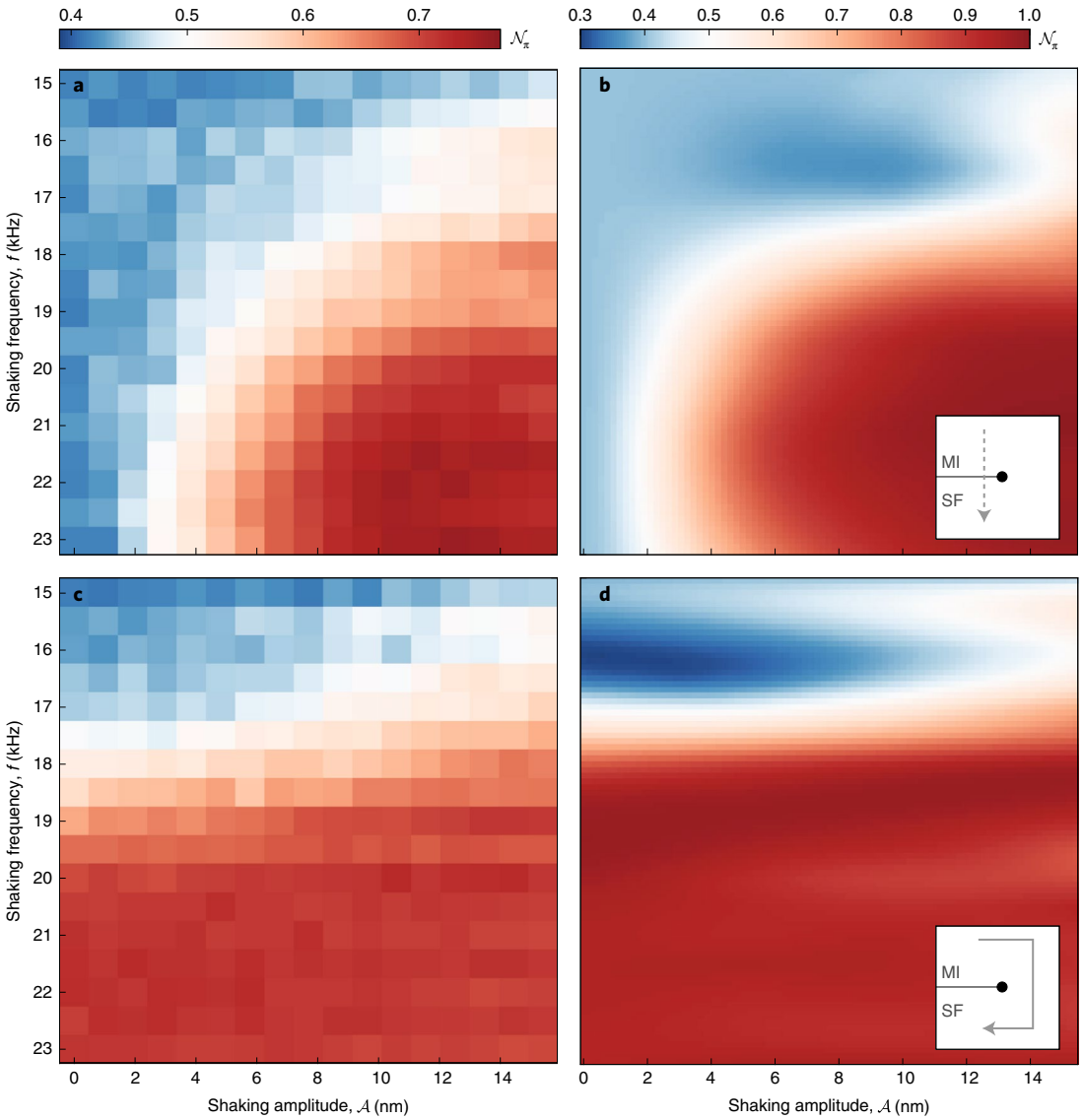


**Fig. 3 | Sweeps across phase transitions and metastability. a**,**b**, Experimental (**a**) and simulated (**b**) band-edge populations $\mathcal{N}_\pi$ following the direct sweeps (inset in (**b**) and dashed arrow in Fig. 2a) as a function of the final amplitude and frequency. **c**,**d**, Corresponding results for indirect sweeps (solid arrow). The direct and indirect sweeps broadly agree in the continuous regime at large amplitudes, but crucially differ in the discontinuous regime. Whereas indirect sweeps always pass through the continuous phase transition where the occupation broadly follows the ground state, the observed populations hardly change during direct sweeps through the discontinuous transition, highlighting the associated metastability. The simulations are based on adaptive tDMRG[38] with the full time-dependent two-band Hamiltonian for ten sites and unity filling (Methods). See Extended Data Fig. 5 for details.

the normalized final momentum distribution $n(k_y)$ after a sweep through the continuous transition from the MI regime ($f_i = 15\,\mathrm{kHz}$) to the π-SF regime ($f_f = 21\,\mathrm{kHz}$) as a function of sweep duration $\tau$, expressed in units of the average drive period $\bar{T} = 2\pi/\bar{f}$, where $\bar{f} := (f_i + f_f)/2$. With increasing $\tau$, prominent peaks emerge at $k_y = \pm k_0$ corresponding to the boundary of the Brillouin zone. The oscillation between $+k_0$ and $-k_0$ stems from the micromotion in the accelerated lattice[10,30] combined with Bragg reflections at the band edge, and the oscillation frequency is equal to $\bar{f}$ (Supplementary Information). The observed dynamics, which is averaged over multiple tubes in the experiment, is in good qualitative agreement with the time-dependent density-matrix renormalization group (tDMRG) simulation at unity filling (Fig. 4b).

We repeat this sweep measurement for different shaking amplitudes (Extended Data Fig. 4) and extract the initial growth rate of the band-edge population, $\partial\mathcal{N}_\pi/\partial\tau$ (Fig. 4c). The vanishing rate of change at weak amplitudes highlights the metastability associated with the discontinuous transition—the system remains in the initial state, even though the phase transition has been crossed. The observed rates are in good agreement with the simulation up to an overall scaling factor that we mainly attribute to the inhomogeneity of the dipole trap. We partially attribute the nonzero susceptibility around the edge of the discontinuous regime to the presence of nucleation points due to initial entropy and boundary effects. We also expect quantum fluctuations to play an important role in this weakly first-order region close to the KT transition, which could be the subject of future studies.

In Fig. 4d, we additionally explore backward sweeps where the system is initially prepared in the π-SF regime ($f_i = 21\,\mathrm{kHz}$) via the continuous phase transition (Fig. 2a, solid arrow) and then swept back to the MI regime ($f_f = 15\,\mathrm{kHz}$). Although the overall structure is very similar to the forward (MI-to-π-SF) sweeps (Fig. 4c), we find an additional small non-zero decay rate that is slightly larger than the independently measured incoherent dephasing rate $\Gamma \approx -65\,\mathrm{s}^{-1}$

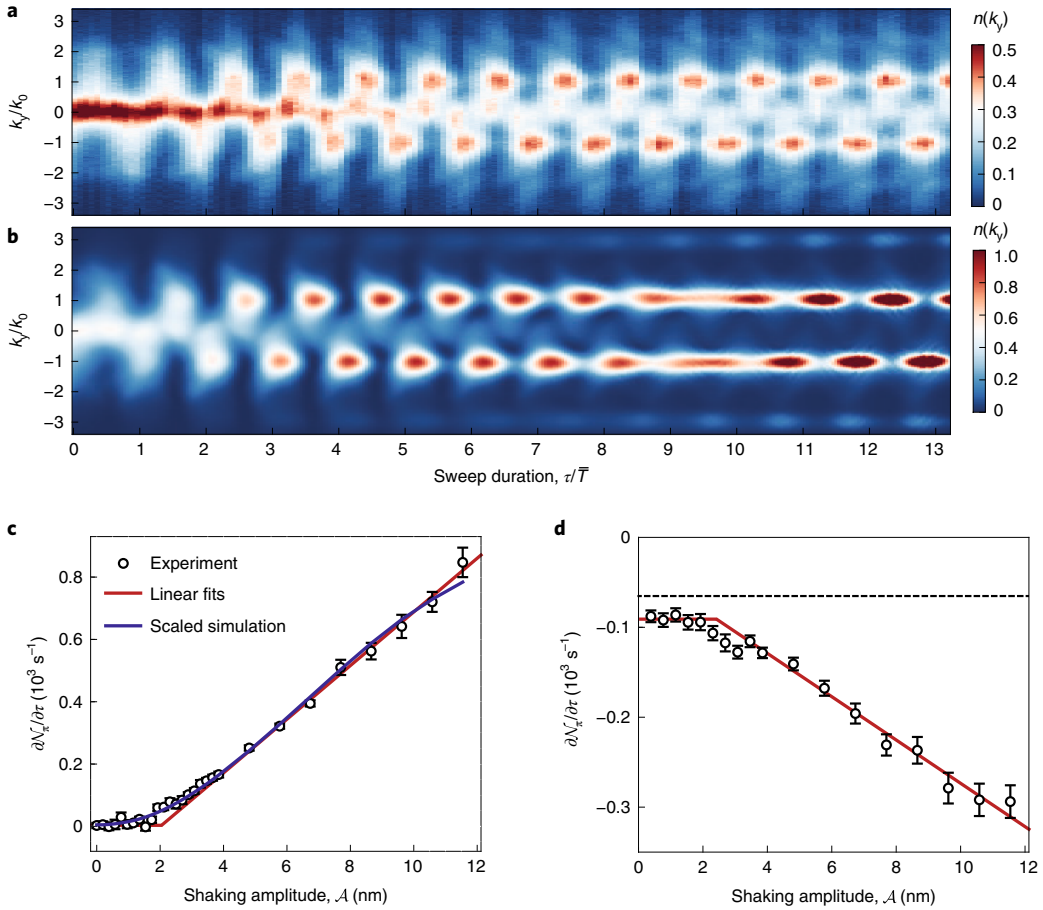


**Fig. 4 | Dynamics of phase transitions. a**,**b**, Normalized experimental (**a**) and simulated (**b**) momentum distributions $n(k_y)$ after a direct frequency sweep from the MI (15 kHz) to π-SF (21 kHz) regime with $\mathcal{A}=11.5$ nm as a function of sweep duration $\tau$. There is an evident build-up of pronounced peaks around $\pm k_0$ along with the induced micromotion. **c**, Initial growth rate of the peaks, $\partial\mathcal{N}_\pi/\partial\tau$, at different shaking amplitudes. In contrast to strong shaking where the rate increases linearly with $\mathcal{A}$, for weak amplitudes, the populations are nearly frozen after crossing the discontinuous phase transition, exhibiting metastability. The red solid line represents a piecewise linear fit and the blue solid line shows the simulation scaled empirically by 0.45 to account for experimental inhomogeneity. **d**, Values of $\partial\mathcal{N}_\pi/\partial\tau$ for backward sweeps, starting from a π-SF (21 kHz) regime prepared via continuous transition back to the MI regime (15 kHz). It also shows metastability for small $\mathcal{A}$, resulting in hysteresis. The black dashed line indicates an incoherent background decay of the π-SF (Supplementary Information). The error bars in **c** and **d** represent the fit uncertainty (one standard deviation) of the fits shown in Extended Data Fig. 4.

(Fig. 4d, dashed line, and Supplementary Information). We attribute this difference to excitations in the prepared π-SF state that could act as nucleation centres. Both forward and backward sweeps demonstrate the metastability and hysteresis associated with the discontinuous transition.

## Conclusion

Using a resonant shaking scheme, we realize a tunable quantum phase transition in an isolated strongly correlated lattice system and demonstrate the strikingly different dynamics of discontinuous and continuous transitions. Ramping across the discontinuous transition reveals the associated quantum metastability, in good agreement with tensor-network simulations. Thus, resonantly driven lattice systems open a new avenue for engineering novel quantum phases and studying genuinely quantum discontinuous transitions and other intriguing critical phenomena. Our technique can be directly extended to higher dimensions where numerical simulations are unfeasible. Future studies can also investigate the decay mechanism of metastable many-body states and explore the emergence of spatial structures resulting from quantum fluctuations and the influence of nucleation points. This will shed light on the dynamics and structure formation in the early Universe[17]. Resonantly driven lattices will furthermore enable novel studies on dynamical scaling across such transitions[8,32–34] and open the door to study prevalent first-order transitions in interacting topological phases[35–37] using quantum simulators.

## Online content

Any methods, additional references, Nature Research reporting summaries, source data, extended data, supplementary information, acknowledgements, peer review information; details of author contributions and competing interests; and statements of data and code availability are available at https://doi.org/10.1038/s41567-021-01476-w.

Received: 22 July 2021; Accepted: 24 November 2021;
Published online: 20 January 2022

## References

1. Coleman, S. Fate of the false vacuum: semiclassical theory. *Phys. Rev. D* **15**, 2929 (1977).
2. Vilenkin, A. Birth of inflationary universes. *Phys. Rev. D* **27**, 2848 (1983).

3. Greiner, M. et al. Quantum phase transition from a superfluid to a Mott insulator in a gas of ultracold atoms. *Nature* **415**, 39–44 (2002).
4. Gross, C. & Bloch, I. Quantum simulations with ultracold atoms in optical lattices. *Science* **357**, 995–1001 (2017).
5. Struck, J. et al. Engineering Ising-XY spin-models in a triangular lattice using tunable artificial gauge fields. *Nat. Phys.* **9**, 738–743 (2013).
6. Trenkwalder, A. et al. Quantum phase transitions with parity-symmetry breaking and hysteresis. *Nat. Phys.* **12**, 826–829 (2016).
7. Campbell, D. et al. Magnetic phases of spin-1 spin–orbit-coupled Bose gases. *Nat. Commun.* **7**, 10897 (2016).
8. Qiu, L.-Y. et al. Observation of generalized Kibble-Zurek mechanism across a first-order quantum phase transition in a spinor condensate. *Sci. Adv.* **6**, eaba7292 (2020).
9. Sträter, C. & Eckardt, A. Orbital-driven melting of a bosonic Mott insulator in a shaken optical lattice. *Phys. Rev. A* **91**, 053602 (2015).
10. Eckardt, A. Colloquium: atomic quantum gases in periodically driven optical lattices. *Rev. Mod. Phys.* **89**, 011004 (2017).
11. Kibble, T. W. Some implications of a cosmological phase transition. *Phys. Rep.* **67**, 183–199 (1980).
12. McLerran, L. The physics of the quark-gluon plasma. *Rev. Mod. Phys.* **58**, 1021 (1986).
13. Sachdev, S. *Quantum Phase Transitions* 2nd edn (Cambridge Univ. Press, 2011).
14. Lifshitz, I. M. & Kagan, Y. Quantum kinetics of phase transitions at temperatures close to absolute zero. *Sov. J. Exp. Theor. Phys.* **35**, 206–214 (1972).
15. Fialko, O. et al. Fate of the false vacuum: towards realization with ultra-cold atoms. *EPL* **110**, 56001 (2015).
16. Fialko, O. et al. The universe on a table top: engineering quantum decay of a relativistic scalar field from a metastable vacuum. *J. Phys. B: At. Mol. Opt. Phys.* **50**, 024003 (2017).
17. Ng, K. L. et al. Fate of the false vacuum: finite temperature, entropy, and topological phase in quantum simulations of the early Universe. *PRX Quantum* **2**, 010350 (2021).
18. Owerre, S. & Paranjape, M. Macroscopic quantum tunneling and quantum–classical phase transitions of the escape rate in large spin systems. *Phys. Rep.* **546**, 1–60 (2015).
19. Osterloh, A. et al. Scaling of entanglement close to a quantum phase transition. *Nature* **416**, 608–610 (2002).
20. Cooper, N. R., Dalibard, J. & Spielman, I. B. Topological bands for ultracold atoms. *Rev. Mod. Phys.* **91**, 015005 (2019).
21. Eckardt, A., Weiss, C. & Holthaus, M. Superfluid-insulator transition in a periodically driven optical lattice. *Phys. Rev. Lett.* **95**, 260404 (2005).
22. Zenesini, A. et al. Coherent control of dressed matter waves. *Phys. Rev. Lett.* **102**, 100403 (2009).
23. Michon, E. et al. Phase transition kinetics for a Bose Einstein condensate in a periodically driven band system. *New J. Phys.* **20**, 053035 (2018).
24. Zheng, W. et al. Strong interaction effects and criticality of bosons in shaken optical lattices. *Phys. Rev. Lett.* **113**, 155303 (2014).
25. Parker, C. V., Ha, L.-C. & Chin, C. Direct observation of effective ferromagnetic domains of cold atoms in a shaken optical lattice. *Nat. Phys.* **9**, 769–774 (2013).
26. Lim, L.-K., Smith, C. M. & Hemmerich, A. Staggered-vortex superfluid of ultracold bosons in an optical lattice. *Phys. Rev. Lett.* **100**, 130402 (2008).
27. Weinberg, M. et al. Multiphoton interband excitations of quantum gases in driven optical lattices. *Phys. Rev. A* **92**, 043621 (2015).
28. Arimondo, E. et al. Kilohertz-driven Bose–Einstein condensates in optical lattices. *Adv. At. Mol. Opt. Phys.* **61**, 515–547 (2012).
29. Schollwöck, U. The density-matrix renormalization group in the age of matrix product states. *Ann. Phys.* **326**, 96–192 (2011).
30. Goldman, N. & Dalibard, J. Periodically driven quantum systems: effective Hamiltonians and engineered gauge fields. *Phys. Rev. X* **4**, 031027 (2014).
31. Clark, L. W., Feng, L. & Chin, C. Universal space-time scaling symmetry in the dynamics of bosons across a quantum phase transition. *Science* **354**, 606–610 (2016).
32. Shimizu, K. et al. Dynamics of first-order quantum phase transitions in extended Bose–Hubbard model: from density wave to superfluid and vice versa. *New J. Phys.* **20**, 083006 (2018).
33. Pelissetto, A., Rossini, D. & Vicari, E. Out-of-equilibrium dynamics driven by localized time-dependent perturbations at quantum phase transitions. *Phys. Rev. B* **97**, 094414 (2018).
34. Coulamy, I. B., Saguia, A. & Sarandy, M. S. Dynamics of the quantum search and quench-induced first-order phase transitions. *Phys. Rev. E* **95**, 022127 (2017).
35. Amaricci, A. et al. First-order character and observable signatures of topological quantum phase transitions. *Phys. Rev. Lett.* **114**, 185701 (2015).
36. Zhao, J., Zhang, Y. & Jain, J. Crystallization in the fractional quantum Hall regime induced by Landau-level mixing. *Phys. Rev. Lett.* **121**, 116802 (2018).
37. Wu, K.-H. et al. Z2 topological order and first-order quantum phase transitions in systems with combinatorial gauge symmetry. *Phys. Rev. B* **104**, 085145 (2021).
38. Paeckel, S. et al. Time-evolution methods for matrix-product states. *Ann. Phys.* **411**, 167998 (2019).

## Methods

**Experimental protocol.** A Bose–Einstein condensate of $1\times10^5$ atoms of $^{87}$Rb in the $|F=1, m_F=-1\rangle$ state is adiabatically loaded into a blue-detuned, simple-cubic three-dimensional lattice. Here $F$ denotes the total angular momentum and $m_F$ the magnetic quantum number of the state. All lattice depths are exponentially increased from zero to their final values in 45 ms with a time constant of 10 ms, resulting in independent 1D MIs. After a hold time of 10–15 ms, we begin to modulate (shake) the position of the $y$ lattice by sinusoidally changing the corresponding laser frequency. To this end, we modulate the radio frequency feeding an acousto-optic modulator in the double-pass configuration. The resulting frequency of the lattice laser $f_l(t)$ becomes

$$f_l(t) = f_c + A_l \sin(2\pi f t), \tag{2}$$

where $f_c$ is the central frequency, $A_l$ is the frequency modulation depth and $f$ denotes the modulation frequency. For a given fixed distance $l_0$ between the atoms and retro-mirror, this frequency modulation results in a time-dependent displacement $s(t) = \mathcal{A}\sin(2\pi f t)$ of the lattice[39], where shaking amplitude $\mathcal{A}$ denotes the maximum displacement of the lattice in space. For the fixed distance between atoms and retro-reflector of $l_0 = 45$ cm and lattice spacing $d = \lambda/2 = 363$ nm in our setup, a frequency modulation amplitude of $A_l = 1$ MHz corresponds to a modulation amplitude of $\mathcal{A} = 3\times10^{-3} d = 1.1$ nm in space. Since the size of the Bose–Einstein condensate is very small compared with $l_0$, inhomogeneity of the shaking amplitude $\mathcal{A}$ across the cloud is less than 0.01%.

The double-pass acousto-optic modulator enables us to control both amplitude and frequency of shaking using a radio-frequency source based on a direct digital synthesis chip. Here we discuss one example of the indirect-sweep protocol used in Fig. 3: we linearly ramp the amplitude from zero to an intermediate value $A_m = 8.8$ MHz in $t_1 = 125$ µs and then the amplitude is kept constant for the next 600 µs until $t_2 = 725$ µs. Finally, the amplitude is linearly changed to the final value, for example, $A_f = 1.7$ MHz at $t_3 = 1{,}025$ µs, as shown in Extended Data Fig. 3a.

$$A_l(t) = \begin{cases} A_m \frac{t}{t_1} & t_1 > t \geq 0 \\ A_m & t_2 > t \geq t_1 \\ (A_f - A_m)\frac{t-t_2}{t_3-t_2} + A_m & t_3 \geq t \geq t_2 \end{cases}. \tag{3}$$

The corresponding frequency variation is given by

$$f(t) = \begin{cases} f_i & t_1 > t \geq 0 \\ (f_f - f_i)\frac{t-t_1}{t_2-t_1} + f_i & t_2 > t \geq t_1 \\ f_f & t_3 \geq t \geq t_2 \end{cases}, \tag{4}$$

where the initial shaking frequency during the first 125 µs is fixed at $f_i = 15$ kHz. Then, the frequency is swept linearly in time (linear chirp) to a final value, for example, $f_f = 21$ kHz in 600 µs (Extended Data Fig. 3b). To guarantee a continuous phase waveform, we apply phase modulation instead of direct frequency control. In this case, equation (2) becomes $f_l(t) = f_c + A_l \sin(\phi(t))$ and the required phase profile is given by $\phi(t) = \int_0^t 2\pi f(t)\mathrm{d}t$, where $f(t)$ denotes the time-dependent modulation frequency and we set the initial phase $\phi_0 = 0$. The resulting time-dependent laser frequency in the indirect sweep is shown in Extended Data Fig. 3c.

In Extended Data Fig. 4, we plot the final population $\mathcal{N}_\pi$ after direct forward sweeps (from the MI to π-SF state) and direct backward sweeps (from the π-SF to MI state). In the forward sweeps, the system is initially prepared in the MI regime ($f_i = 15$ kHz) and we measure $\mathcal{N}_\pi$ as a function of duration $\tau$ of the frequency sweep to the final shaking frequency ($f_f = 21$ kHz). In the backward sweeps, the system is first prepared in the π-SF regime ($f_i = 21$ kHz) following the indirect-sweep protocol, before sweeping the shaking frequency back to $f_f = 15$ kHz over different sweep durations.

**Band-edge population $\mathcal{N}_\pi$.** We extract the (normalized) population at the band edge $\mathcal{N}_\pi := n_\pi/(n_0 + n_\pi)$ by directly counting the numbers of atoms in fixed boxes around $k_y = 0$ (for $n_0$) and $k_y = \pm k_0$ (for $n_\pi$) (Extended Data Fig. 5a). This image is averaged over 30 experimental repetitions, demonstrating the stability of peak positions. The same data are shown in Fig. 1e. To evaluate the robustness of this analysis method, we vary the width of the boxes ($l_{\mathrm{box}}$) along the modulated $k_y$ direction. Extended Data Fig. 5b–f shows the extracted populations following the direct sweeps from Fig. 3 for box widths $l_{\mathrm{box}}$ ranging from $0.1k_0$ to $0.8k_0$. Although the absolute value of $\mathcal{N}_\pi$ is modestly dependent on $l_{\mathrm{box}}$, the observed pattern is robust and insensitive to the box width. In Figs. 3 and 4, we have used $l_{\mathrm{box}} = 0.6k_0$.

**Extended Hubbard model.** In the moving frame of the lattice, the system is described by an effective 1D Hamiltonian

$$\hat{H}(t) = \int \mathrm{d}y \,\{\, \hat{\psi}^\dagger(y)\left[-\tfrac{\hbar^2}{2m}\partial_y^2 + V_{\mathrm{lat}}(y) + F(t)y\right]\hat{\psi}(y) + \tfrac{g_{1D}}{2}\hat{\psi}^\dagger(y)\hat{\psi}^\dagger(y)\hat{\psi}(y)\hat{\psi}(y)\,\}\,, \tag{5}$$

where $\hat{\psi}(y)$ is the boson field operator, $m$ is the mass, $V_{\mathrm{lat}}(y) = V_0\sin^2(\pi y/d)$ is the unperturbed lattice potential and $g_{1D}$ is an effective interaction strength. Further, $F(t) = m\ddot{s}(t)$ is an inertial periodic force arising from displacement $s(t)$ due to shaking, which resonantly couples the two lowest bare bands of the lattice. We approximate the field operator in terms of the localized Wannier functions in these two bands as follows:

$$\hat{\psi}(y) = \sum\nolimits_j w_1(y - y_j)\,\hat{a}_j + w_2(y - y_j)\,\hat{b}_j\,, \tag{6}$$

where $\hat{a}_j$ and $\hat{b}_j$ are the corresponding bosonic annihilation operators. Substituting this expansion into equation (5) and retaining the most significant terms for a deep lattice, one obtains (up to a constant energy shift)

$$\begin{aligned}\hat{H}(t) = {} & \Delta_E \sum_j \hat{b}_j^\dagger\hat{b}_j - J_a\sum_{\langle i,j\rangle}\hat{a}_i^\dagger\hat{a}_j + J_b\sum_{\langle i,j\rangle}\hat{b}_i^\dagger\hat{b}_j + J_b'\sum_{\langle\langle i,j\rangle\rangle}\hat{b}_i^\dagger\hat{b}_j \\ & + F(t)d\left[\sum_j j(\hat{a}_j^\dagger\hat{a}_j + \hat{b}_j^\dagger\hat{b}_j) + \alpha_{ab}\sum_j \hat{a}_j^\dagger\hat{b}_j + \hat{b}_j^\dagger\hat{a}_j\right] \\ & + \tfrac{U_a}{2}\sum_j \hat{a}_j^\dagger\hat{a}_j^\dagger\hat{a}_j\hat{a}_j + \tfrac{U_b}{2}\sum_j \hat{b}_j^\dagger\hat{b}_j^\dagger\hat{b}_j\hat{b}_j + U_{ab}\sum_j \hat{a}_j^\dagger\hat{b}_j^\dagger\hat{b}_j\hat{a}_j \\ & + \tfrac{U_{ab}}{4}\sum_j(\hat{a}_j^\dagger\hat{a}_j^\dagger\hat{b}_j\hat{b}_j + \text{h.c.})\,,\end{aligned} \tag{7}$$

where $\Delta_E := \varepsilon_b - \varepsilon_a$, $\varepsilon_{a,b}$ are the average energies of the two bands, $\langle\langle i,j\rangle\rangle$ denotes the next-nearest neighbours and $\alpha_{ab}$ is the coupling amplitude between the two bands. The energy scales appearing in equation (7) can be calculated using the dispersion and Wannier functions of the energy bands, which are given by Mathieu functions[40]. For our experimental parameters, $\Delta_E = 19.7$ kHz, $J_a = 0.12$ kHz, $J_b = 1.29$ kHz, $J_b' = 0.17$ kHz, $U_a = 2.88$ kHz, $U_b = 1.73$ kHz, $U_{ab} = 2.36$ kHz and $\alpha_{ab} = 0.15$ (all the energies are expressed in units of frequency).

In a single-band Hubbard model, the MI–SF transition is known to occur at $J/U \approx 0.3$[41]. Thus, in our setup, the ground state of the lower band is an MI state ($J_a/U_a \approx 0.04$), whereas that of the upper band is a π-SF state ($J_b/U_b \approx 0.74$). To simulate the experimental sweeps, we evolve the time-dependent Hamiltonian in equation (7) with ten particles on ten sites using an adaptive tDMRG routine[42]. We use a fourth-order Euler stepper with a time step of 0.05 µs, keeping singular values above $10^{-10}$, with a maximum bond dimension of 100 and up to four particles per site, for which the results converge. The above approach can also be extended to incorporate corrections from higher bands (Supplementary Section IV provides the simulation of sweeps including the third (second excited) band).

For a constant periodic drive, $F(t) = -m\omega^2\mathcal{A}\sin\omega t$, where $\omega \equiv 2\pi f$, a simpler description can be found in the rotating frame via the transformation $\hat{R} = \mathrm{e}^{\mathrm{i}\omega t\sum_j \hat{b}_j^\dagger\hat{b}_j}$, which gives $\hat{R}\hat{b}_j\hat{R}^\dagger = \mathrm{e}^{-\mathrm{i}\omega t}\hat{b}_j$ and $\hat{R}[\mathrm{i}\hbar\partial_t - \hat{H}(t)]\hat{R}^\dagger \equiv \mathrm{i}\hbar\partial_t - \hat{H}_{\mathrm{rot}}$, where $\hat{H}_{\mathrm{rot}}$ is the rotating-frame Hamiltonian. Using equation (7) yields

$$\hat{H}_{\mathrm{rot}} = \hat{H}_0 + \left(\hat{H}_1\mathrm{e}^{\mathrm{i}\omega t} + \hat{H}_2\mathrm{e}^{\mathrm{i}2\omega t} + \text{h.c.}\right)\,, \tag{8}$$

where $\hat{H}_0$, $\hat{H}_1$ and $\hat{H}_2$ are time independent. For a sufficiently deep lattice, the terms within the parentheses represent fast oscillations, since $\omega$ is close to the bandgap. One can find an effective (Floquet) Hamiltonian $\hat{H}_{\mathrm{eff}}$ that generates the time-averaged dynamics by using a high-frequency Magnus expansion[30]. For $\omega \to \infty$, this is simply $\hat{H}_0$. For finite $\omega$, the most important correction comes from the oscillatory force given by $\hat{H}_1$, which renormalizes the hopping amplitudes. Retaining all the other terms of order $1/\omega$, we find

$$\begin{aligned}\hat{H}_{\mathrm{eff}} = {} & -J_a\mathcal{J}_0(\eta)\sum_{\langle i,j\rangle}\hat{a}_i^\dagger\hat{a}_j + J_b\mathcal{J}_0(\eta)\sum_{\langle i,j\rangle}\hat{b}_i^\dagger\hat{b}_j + J_b'\mathcal{J}_0(2\eta)\sum_{\langle\langle i,j\rangle\rangle}\hat{b}_i^\dagger\hat{b}_j \\ & + \sum_j \Delta_{\mathrm{eff}}\,\hat{b}_j^\dagger\hat{b}_j + (\Omega/2)\left(\hat{a}_j^\dagger\hat{b}_j + \hat{b}_j^\dagger\hat{a}_j\right) \\ & + \sum_j \tfrac{U_a^{\mathrm{eff}}}{2}\hat{a}_j^\dagger\hat{a}_j^\dagger\hat{a}_j\hat{a}_j + \tfrac{U_b^{\mathrm{eff}}}{2}\hat{b}_j^\dagger\hat{b}_j^\dagger\hat{b}_j\hat{b}_j + U_{ab}\,\hat{a}_j^\dagger\hat{b}_j^\dagger\hat{b}_j\hat{a}_j \\ & + \tfrac{U_{ab}^2}{8\hbar\omega}\hat{n}_j^a\hat{n}_j^b(\hat{n}_j^b - \hat{n}_j^a) + \tfrac{\Omega U_{ab}}{8\hbar\omega}\left[\hat{a}_j^\dagger(\hat{n}_j^b - \hat{n}_j^a)\hat{b}_j + \text{h.c.}\right],\end{aligned} \tag{9}$$

where $\eta := F_0 d/(\hbar\omega)$, $F_0 := m\omega^2\mathcal{A}$, $\mathcal{J}_0$ is the Bessel function of the first kind, $\Omega := F_0 d\alpha_{ab}$ is the Rabi frequency, $\Delta_{\mathrm{eff}} := \Delta_E - \hbar\omega + \Omega^2/(4\hbar\omega)$ is an effective detuning, $U_a^{\mathrm{eff}} := U_a - U_{ab}^2/(8\hbar\omega)$ and $U_b^{\mathrm{eff}} := U_b + U_{ab}^2/(8\hbar\omega)$ are the effective interaction energies, $\hat{n}_j^a := \hat{a}_j^\dagger\hat{a}_j$, and $\hat{n}_j^b := \hat{b}_j^\dagger\hat{b}_j$. For a typical shaking frequency $f = 18$ kHz and amplitude $\mathcal{A} = 5$ nm, $F_0 d = 5$ kHz, $\eta = 0.3$, $\Omega = 0.75$ kHz, $U_{ab}/(\hbar\omega) = 0.1$ and $\Omega/(\hbar\omega) = 0.04$; therefore, the corrections coming from $\hat{H}_1$ and $\hat{H}_2$ are small in the experiment. In particular, $\mathcal{J}_0(0.3) \approx 0.98$; hence, the resulting renormalization of the tunnelling elements can be neglected. Together with ignoring the second-order hopping $J_b'$, these simplifications reduce $\hat{H}_{\mathrm{eff}}$ to the Hamiltonian in equation (1). We calculate the effective phase diagram (Fig. 2 and Supplementary Fig. S3a) by minimizing $\hat{H}_{\mathrm{eff}}$ for unity filling using two-site DMRG[29] with open boundary conditions, singular value cutoff of $10^{-8}$, maximum bond dimension of 200, and up to four particles per site.

**Phase boundary.** To characterize the ground states of $\hat{H}_{\mathrm{eff}}$ with $L$ sites, we find the single-particle correlations in the bulk, for example, $\langle\langle \hat{b}_i^\dagger \hat{b}_{i+r}\rangle\rangle$, by discarding $L/4$ sites from either end and averaging over all the remaining pairs of sites with separation $r$ (double brackets in this section denote such bulk averaging). We find that these correlations are well fitted by $|\langle\langle \hat{b}_i^\dagger \hat{b}_{i+r}\rangle\rangle| \approx Cr^{-1/(2K)}\mathrm{e}^{-r/\xi}$ (similarly for $\langle\langle \hat{a}_i^\dagger \hat{a}_{i+r}\rangle\rangle$), where $\xi$ is the correlation length and $K$ is an effective Luttinger parameter (Extended Data Fig. 1a). In the MI phase, $\xi$ is finite and the correlations decay exponentially at large distances. In the SF phase, $\xi$ becomes much larger than $L$ and the correlations follow a power law set by the drive parameters. At weak shaking amplitudes, both $\xi$ and $K$ jump discontinuously across a first-order transition (Extended Data Fig. 1b), whereas at large amplitudes, they continuously vary across a KT transition (Extended Data Fig. 1c). For very strong shaking ($\mathcal{A} \to \infty$), the KT transition occurs in a single hybridized band at $K = 2$[43].

To determine the phase boundary more robustly, we analyse the bipartite entanglement in the ground state that shows universal scaling close to a critical point in which the system maps onto a conformal field theory[44]. In particular, the von Neumann entanglement entropy between the first $i$ sites and the remaining $L-i$ sites is

$$S_{\mathrm{vN}} = \frac{c}{6}\log\left[\frac{L}{\pi}\sin\left(\frac{\pi i}{L}\right)\right] + c_1\,, \tag{10}$$

where $c_1$ is a non-universal constant and $c$ is called a central charge that determines how strongly the entanglement entropy varies near $i = L/2$.

As shown in Extended Data Fig. 2a, the bulk entropy variation (for $L = 64$) is very well approximated by equation (10), where $c$ and $c_1$ are fit parameters. The fitted charge $c$ is 0 well inside the MI phase and 1 well inside the SF phase. For weak amplitudes (Extended Data Fig. 2b), this change discontinuously occurs across a first-order transition where $c$ jumps from 0 to its maximum value, coinciding with the jump in the one-body correlation lengths (Extended Data Fig. 1b). On the other hand, the large-amplitude variation (Extended Data Fig. 2f) is continuous and exhibits a smooth peak, similar to what happens for an MI–SF transition in a single band[41]. As argued in ref. [41], the critical point can be traced to the location of this maximum. For intermediate amplitudes, the behaviour is more complicated. In Extended Data Fig. 2c, both jump and smooth peak are evident, signalling two back-to-back phase transitions in which the intervening phase is a staggered MI (Supplementary Section III). The tracing of these peaks and jumps leads to the full phase diagram (Supplementary Fig. S3a).

## Data availability

The data for all figures that support the findings of this study are available in Hierarchical Data Format (HDF5) at the Apollo repository (https://doi.org/10.17863/CAM.78025)

## Code availability

The code that supports the plots in this paper is available from the corresponding author upon reasonable request.

## References


39. Fölling, S. et al. Direct observation of second-order atom tunnelling. *Nature* **448**, 1029–1032 (2007).
40. Drese, K. & Holthaus, M. Ultracold atoms in modulated standing light waves. *Chem. Phys.* **217**, 201–219 (1997).
41. Ejima, S. et al. Characterization of Mott-insulating and superfluid phases in the one-dimensional Bose-Hubbard model. *Phys. Rev. A* **85**, 053644 (2012).
42. Paeckel, S. et al. Time-evolution methods for matrix-product states. *Ann. Phys.* **411**, 167998 (2019).
43. Rachel, S. et al. Detecting quantum critical points using bipartite fluctuations. *Phys. Rev. Lett.* **108**, 116401 (2012).
44. Calabrese, P. & Cardy, J. Entanglement entropy and quantum field theory. *J. Stat. Mech.* **2004**, P06002 (2004).


## Acknowledgements


This work was partly funded by the European Commission ERC Starting Grant QUASICRYSTAL, the EPSRC Grant EP/R044627/1 and Programme Grant DesOEQ (EP/P009565/1), and by a Simons Investigator Award. We are grateful to E. Gottlob and A. Eckardt for fruitful discussions.


## Author contributions

N.C. and U.S. conceived and supervised the project, with S.D. and B.S. leading the detailed design. B.S., S.B., J.-C.Y. and E.C. performed the experiments. B.S. analysed the experimental data and S.D. performed the numerical simulations. All the authors contributed to the interpretation of the results and writing of the manuscript.

## Competing interests

The authors declare no competing interests.

## Additional information

**Extended data** is available for this paper at https://doi.org/10.1038/s41567-021-01476-w.

**Supplementary information** The online version contains supplementary material available at https://doi.org/10.1038/s41567-021-01476-w.

**Correspondence and requests for materials** should be addressed to Ulrich Schneider.

**Peer review information** *Nature Physics* thanks the anonymous reviewers for their contribution to the peer review of this work.

**Reprints and permissions information** is available at www.nature.com/reprints.

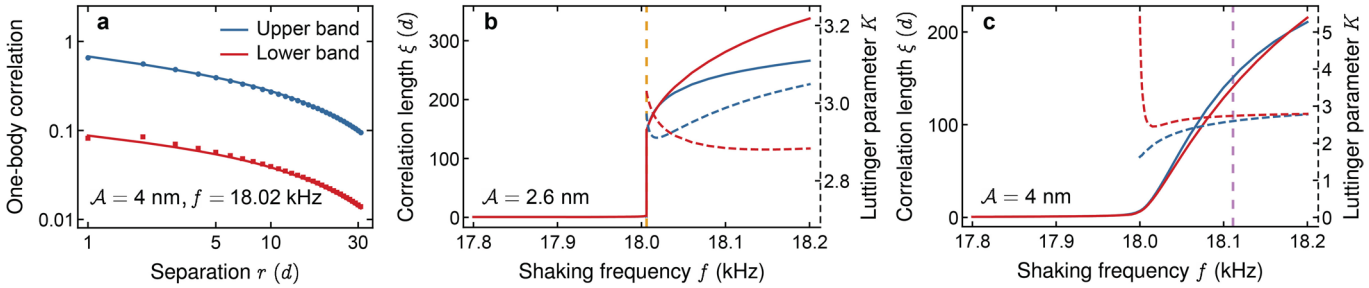


**Extended Data Fig. 1 | Single-particle correlations. a**, Average correlations $\langle\langle \hat{a}_i^\dagger \hat{a}_{i+r} \rangle\rangle$ and $|\langle\langle \hat{b}_i^\dagger \hat{b}_{i+r} \rangle\rangle|$ in the ground state with $L = 64$ sites, fitted with an exponential times a power law. **b-c**, Correlation length (solid lines) and Luttinger parameter (dashed lines) extracted from the fits across first-order and continuous transitions denoted by vertical lines (cf. Extended Data Fig. 2).

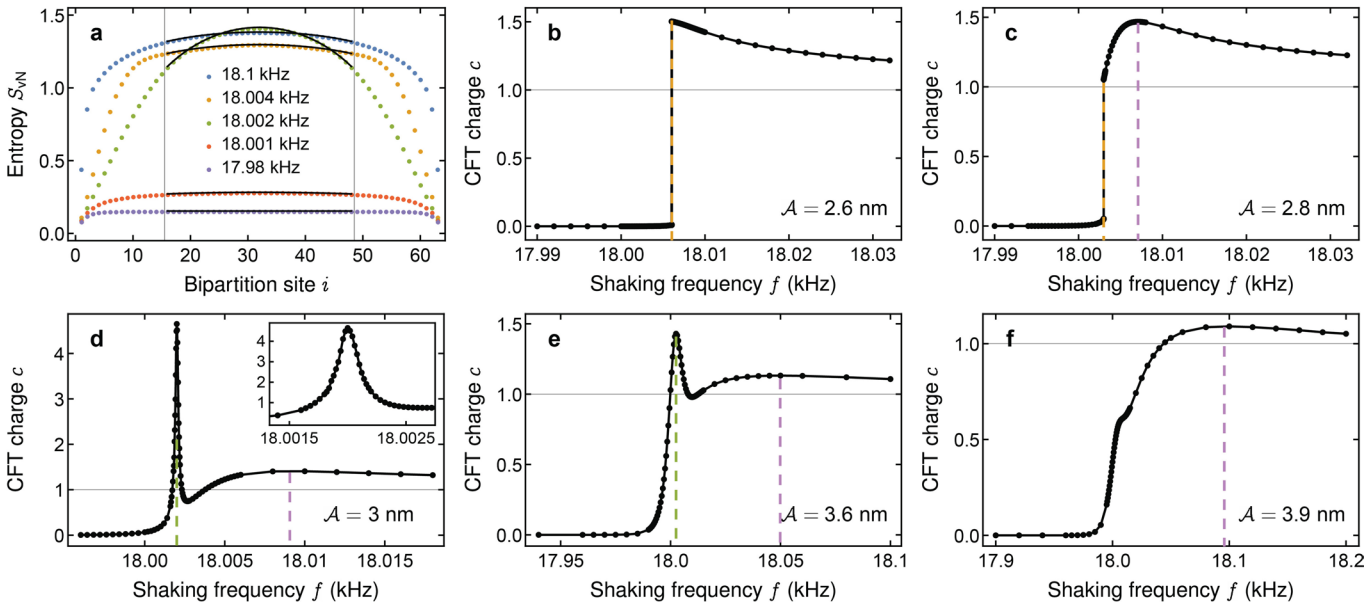


**Extended Data Fig. 2 | Entanglement and central charge. a**, Von Neumann entanglement entropy across bipartitions of the ground state for $L = 64$ and $\mathcal{A} = 3$ nm with different shaking frequencies, fitted with the conformal field theory (CFT) prediction in Eq. (10). **b-f**, Fitted central charge $c$ as a function of the shaking frequency at increasing shaking amplitudes, exhibiting discontinuous jumps and smooth peaks characteristic of discontinuous (first-order) and continuous phase transitions, respectively (shown by the vertical dashed lines, with the same color convention as in the phase diagram in Supplementary Fig. S3).

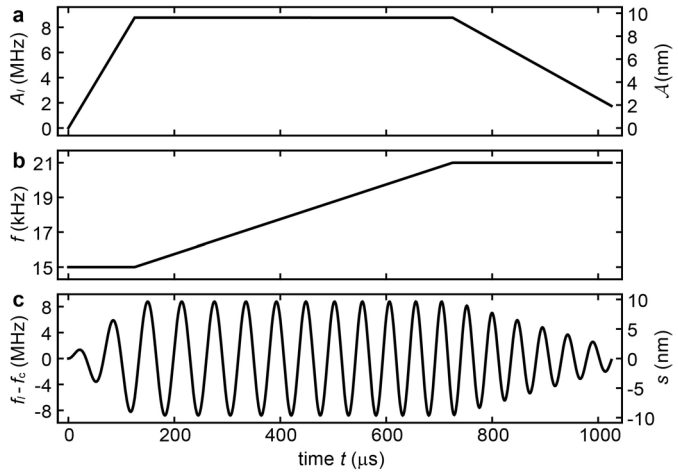


**Extended Data Fig. 3 | Frequency modulation of lattice laser.** An example of the indirect sweep sequence with a final shaking frequency $f_f = 21$ kHz and a final shaking amplitude $\mathcal{A} = 1.9$nm. **a**, **b** and **c** show variations of the modulation depth $A_l$ (the shaking amplitude $\mathcal{A}$), the shaking frequency $f$ and the laser frequency $f_l$ (the displacement of the lattice $s$), respectively.

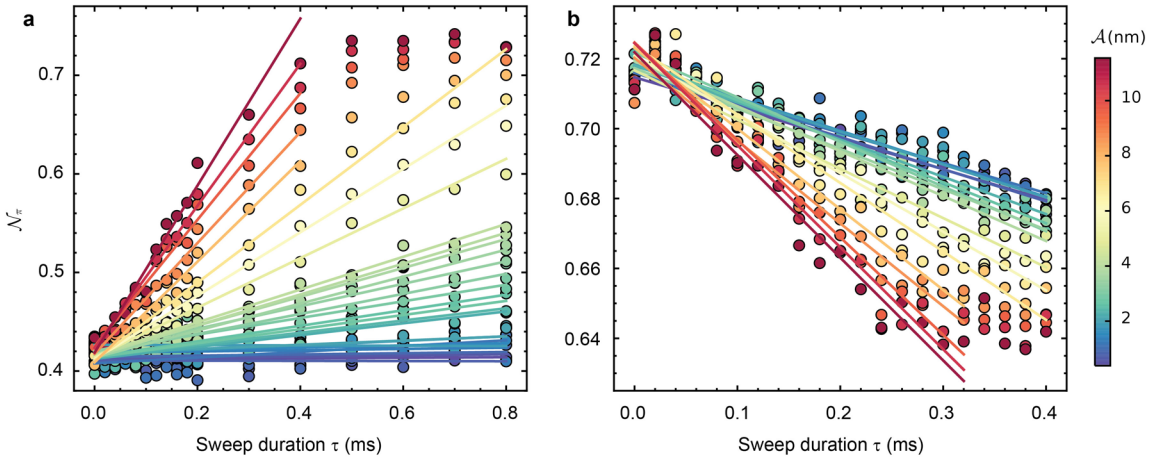


**Extended Data Fig. 4 | Measured band-edge population after different sweep durations for different shaking amplitudes. a** and **b** show the final population $\mathcal{N}_\pi$ after direct sweeps in the forward (from a MI to a $\pi$-SF state) and backward (from a $\pi$-SF to a MI state) directions, respectively. We extract $\partial\mathcal{N}_\pi/\partial\tau$ by the linear fits (solid lines). The fit results are shown in Fig. 4c,d.

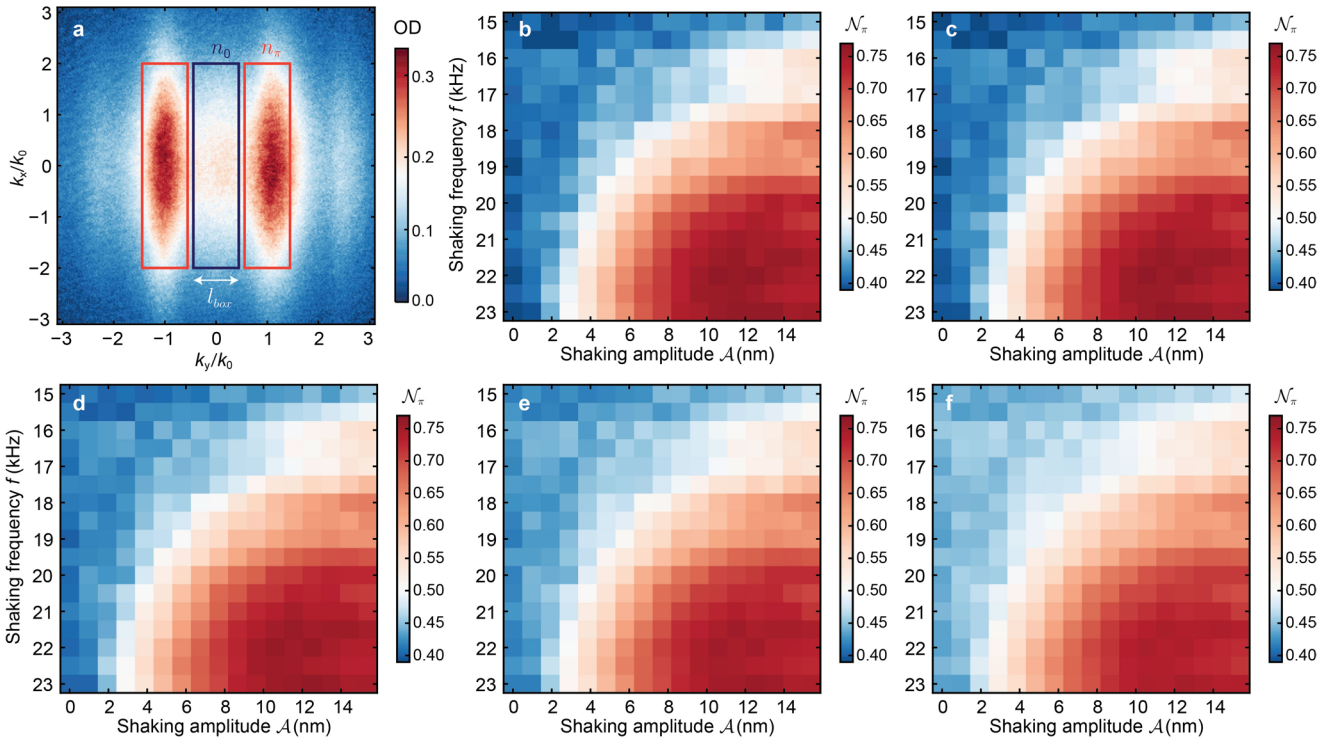


**Extended Data Fig. 5 | The band-edge population $\mathcal{N}_\pi$.** (**a**) Atom numbers around $k=0$ ($n_0$) and $k=\pm k_0$ ($n_\pi$) are counted inside the boxes in blue and red, respectively. Note that $n_\pi$ is the sum over the two red boxes. (**b**-**f**) are measured with different box sizes $l_{box}/k_0 = 0.1, 0.2, 0.4, 0.6$, and $0.8$, respectively.